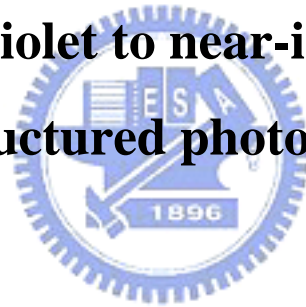


國立交通大學
光電工程研究所

碩士論文

紫外至可見光之奈米結構光偵測器

**Ultraviolet to near-infrared
nanostructured photodetectors**



研究生：李卓奕

指導教授：郭浩中教授

盧廷昌教授

中華民國九十六年六月

紫外至紅外光之奈米結構光偵測器

學生：李卓奕

指導教授：郭浩中教授

盧廷昌教授

國立交通大學光電工程研究所碩士班

摘 要

本論文研究雙極的 MOS (metal-oxide-semiconductor) 結構增益型光偵測器的光響應情形，同時對此一元件的光電轉換機制作進一步的探討。在逆偏壓下，340-1000 nm波段的光都可觀察到有響應電流，最高光電轉換效率可達138%，其可解釋為此奈米量子點光偵測器操作在逆偏壓時，由於矽基底形成反轉層，且其上之奈米結構膜會捕獲正電荷而增強載子由反轉層注入到上電極，此效應如同電晶體中載子由射極注入到集極。最終形成奈米膜中產生之光激電流被放大之效應。

Ultraviolet to Near-infrared nanostructured photodetector

Student: Juo-Yi Lee

Advisor: Dr. Hao-Chung Kuo

Dr. Tien-Chang Lu

Institute of Electro-Optical Engineering

National Chiao Tung University

Abstract

In this thesis, we constructed a two-terminal metal-oxide-semiconductor photodetector for which light is absorbed in a capping layer of silicon nanocrystals embedded in a mesoporous silica matrix on *p*-type silicon substrates. Operated at reverse bias, enhanced photoresponse from 340 to 1000 nm was observed. The highest optoelectronic conversion efficiency is as high as 138%. The enhancements were explained by a transistorlike mechanism, in which the inversion layer acts as the emitter and trapped positive charges in the mesoporous dielectric layer assist carrier injection from the inversion layer to the contact, such that the primary photocurrent could be amplified.

誌謝

本論文能夠順利完成，首先要感謝我的指導老師郭浩中教授及盧廷昌教授，使我在兩年的研究所學習生涯中，得以培養出獨立研究的能力。特別感謝國家奈米元件實驗室謝嘉民博士給予我悉心的指導與鼓勵，讓我知道實驗的方向及效率是影響成果優劣的最重要因素。其次，也要謝謝王興宗教授及余沛慈教授擔任我的口試委員，提供我不少的寶貴意見。

感謝奈米元件實驗室工程師賴一凡及王昭凱學長在實驗上對我的指導，你們的經驗與指教幫助我度過不少難關。感謝博士班學長們忻宏學長、怡超學長、小強學長、小朱學長、泓文學長、宗憲學長、小賴學長、乃方學姊、清華學長、明華學長、俊榮學長、士偉學長的討論與指教，你們的指點幫忙讓我的研究更加順利。感謝和我共同奮鬥的同學們：家璞、立凡、孟儒、潤琪、瑞農、碩均，真的很慶幸能遇見你們這群可愛的朋友，有你們的陪伴，兩年的生活更加多采多姿。也謝謝士嘉、建達及所有學弟妹默默地付出，使我能順利的完成研究。祝福你們未來的研究順利。

最後，謹將本論文獻給我的家人。謝謝他們兩年來的支持與鼓勵，使我能順利完成學位。

Contents

Abstract (in Chinese)	i
Abstract (in English)	ii
誌謝	iii
Contents	iv
List of Table	vi
List of Figures	vii
Chapter 1 Introduction	1
1.1 Review works	1
1.2 Motivation	3
1.3 References	5
Chapter 2 Basic Theory about Photodetector	7
2.1 Schottky contact	7
2.2 Schottky barrier photodiodes	9
2.3 Quantum Efficiency	12
2.4 Responsivity	13
2.5 Gain effect	14
2.6 Detectivity	15
2.7 C-V measurement	16
2.8 References	19
Chapter 3 Experimental Detail	20
3.1 Process	20
3.1.1 Preparation of mesoporous silica template	20
3.1.2 The growth of 3-D Si (and Ge) nanocrystals by HDP-CVD	22
3.1.3 Device fabrication	24

3.2 Experiment Setup	25
3.2.1 The Capacitance-Voltage measurement system	25
3.2.2 Spectral responsivity measurement system	26
3.3 References	27
Chapter 4 Results and Discussions	28
4.1 TEM Image	28
4.2 C-V Measurement	29
4.3 I-V characteristics of the photodetector	32
4.4 Results of Spectral response	34
4.5 Amplified current caused by barrier lowering of transistor	36
4.5.1 Bipolar junction transistor	36
4.5.2 Phototransistor	37
4.5.3 Transistor-like mechanism	38
4.6 References	41
Chapter 5 Conclusions and future works	42
5.1 Conclusions	42



List of Table

Table I Comparison with other researches about UV photodetectors.....2



List of Figures

Fig. 2.1 Energy-band diagram of a metal and semiconductor before contact.....	7
Fig. 2.2 Ideal energy-band diagram of a metal- semiconductor junction for $\Phi_m > \Phi_s$...	8
Fig. 2.3 The mechanisms of current transport in forward-biased Schottky contact.....	9
Fig. 2.4 Energy-band diagram of a forward-biased metal-semiconductor junction including the image lowering effect.....	10
Fig. 2.5 (a) Energy-band diagram through an MOS capacitor for the accumulation mode. (b) Differential charge distribution at accumulation for a differential change in gate voltage.....	16
Fig. 2.6 (a) Energy-band diagram through an MOS capacitor for the inversion mode. (b) Differential charge distribution at inversion for a differential change in gate voltage (high frequency)	17
Fig. 3.1 Flowchart of sol-gel procedure for preparing mesoporous silica nanotemplate films.	21
Fig. 3.2 Schematic mechanism of 3D Si nanodots formed by pulse ICP process.....	23
Fig. 3.3 A schematic drawing illustrating the configuration of the photodiodes of ITO/nc-Si embedded MS / <i>p</i> -Si.	24
Fig. 3.4 The schematic diagram of C-V measurement system.....	25
Fig. 3.5 Diagram of spectral responsivity measurement system.....	26
Fig. 4.1 The cross-sectional TEM images of the mesoporous silica (MS) films with high density silicon nanocrystals.....	28
Fig. 4.2 (a) A schematic drawing illustrate the configuration of the device with compound oxide. (b) The image shows device with Al contact layer.....	29
Fig. 4.3 High frequency C-V characteristics of the sample (a) with Si QD and (b) Ge QD imbedded in MS.	30
Fig. 4.4 The dependence of the memory window, i.e., the flatband shift on	

programming voltage. There are multilevel charge storage in mesoporous silica matrix with Ge nanocrystals.31

Fig. 4.5 A schematic drawing illustrating the structure of MS/ p-Si.....33

Fig 4.6 Current-voltage characteristics of (a) ITO/nc-Si-embedded MS/*p*-Si and (b) ITO/nc-Ge-embedded MS/*p*-Si devices under dark and under illumination at wavelength from 340 to 1000-nm.33

Fig. 4.7 Spectral dependence of the photoresponse of detectors with ITO/nc-Si-embedded MS / *p*-Si, ITO/nc-Si-embedded MS/ *p*-Si , ITO/MS/*p*-Si structures and typical spectral response for Silicon and Germanium.35

FIG. 4.8 (a) Biasing and carrier distribution of an npn BJT in the forward-active mode. (b) The principle of operation of the phototransistor.....36

FIG. 4.9 Illustration of transistor like operation of an ITO/nc- Si-embedded MS/*p*-Si device under reverses bias. (a) A schematic band diagram before illumination and (b) under illumination.39

FIG. 4.10 A schematic band diagram of an ITO/ nc-Si(Ge)-embedded MS/ *p*-Si device under forward bias.....40

Chapter 1 Introduction

1.1 Review works

Photovoltaic devices are essential components in photonics [1] and solar-cells [2], as well as even bio-chips [3]. Bulk silicon, which exhibited impressed success in electronics, with indirect narrow band-gap of 1.1 e V, fails to complete with direct wide band-gap materials on applications in ultraviolet –near infrared light detection.

Near-infrared has many applications such as Astronomical spectroscopy, remote monitoring, and medical diagnostics. And ultraviolet light recently face an intense demand in optical storage systems [4]. Nanostructures, unlike bulk materials, exhibited size-dependent electronic states [5]. Recent research has shown that reducing the size of a Si crystal to a few tens of atoms effectively creates a “direct” wide-bandgap material [6,7]. Contrary to bulk Si or large particles, the electron hole pairs do not appreciably recombine via nonradiative processes, allowing charge separation and collection.

Specific techniques such as electrochemical etching [8,9] or porous silicon [10,11] are proposed to prepare ultrasmall Si nano-particles or nano-channels with direct wide-bandgap characteristics for Si based detector fabrication. With such a material, they demonstrated the Si nano-structured ultraviolet photodetector by processes which are complex, hard to be controlled, and not fully compatible with the conventional IC processing lines. **Table 1** list the characteristics of comparison with other researches about photodetectors.

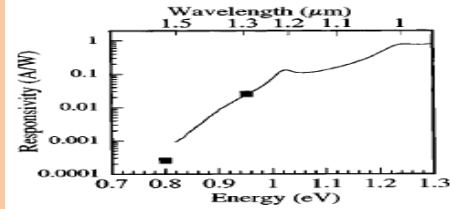
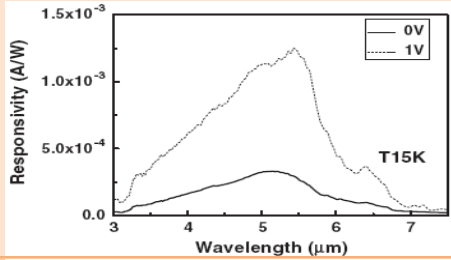
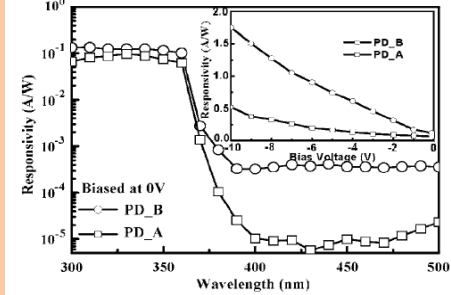
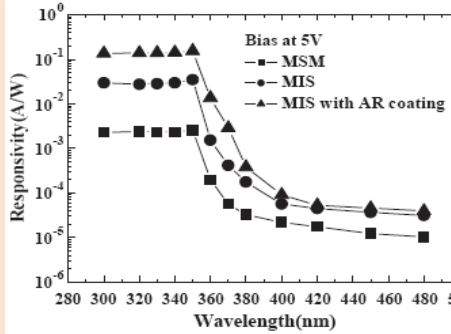
Material structure	Responsivity (A/W)	
<i>Ge/Si (p-i-n)</i> [12]	0.9 at 1000nm 0.1 at 1200nm	
<i>Ge /Si (MOS)</i> [13]	1.2×10^{-3} at 5.7 μm	
<i>GaN (pn)</i> [14]	0.01 at 270nm	
<i>GaAs / AlGaAs quantum well</i> [15]	0.12 at 350nm	

Table 1 Comparison with other researches about photodetectors.

1.2 Motivation

Since the discovery of highly efficient photoluminescence (PL) in the visible region from nanometer-sized silicon crystallites (Si nanodot) [16], extensive study on the Si nanodots has been stimulated by their possibility as a light emitting material. At the same time, the Si nanodots are expected to be a photoconductive material for the following reasons: (1) The spectral response characteristics are controlled by changing the band gap with the crystal size of the Si nanodot. (2) The impact ionization rate of the single crystal Si nanodot must be higher than that of amorphous Si and amorphous Si. (3) When a semi-ballistic carrier transport [17] in the Si-nanodot/SiO₂ system occurs, the impact ionization rate is expected to be higher than that of the single crystal Si.

Because the dot size fluctuation brings about a variation in the band gap of the dots. To obtain high photosensitivity for stacked layer structures of Si nanodots, controlling the dot density and the oxide thickness are of great importance, because the electron tunneling between neighboring Si nanodots limits the transport of the photoexcited carriers. In addition, because defects such as Si dangling bonds act as non-radiative recombination centers of the photoexcited carriers, the low defect density is also a crucial factor.

We reported that self-assembled mesoporous silica (MS) with extremely large internal surface area recently. The dielectric constant and reliability of MS films as interlayers strongly depend on their porosity and the amount of moisture taken up [18]. In considering the number of radiative recombination centers within the MS matrix, the porosity (or pore nanostructures) determines the total area of the pore-surfaces (and, thus, the abundances of the emission centers [19-23]) and the nanoscaled surroundings, both of

which influence the luminescence efficiency and spectra. The advantages of MS film are high porosity (30~75%), controllable pore diameter (2~10nm), ordering pore channel array, and providing quantum surrounding for doping nanomaterials.

At the nanometer scale, the ratio of the numbers of atoms on the surface and in the bulk of a material increases rapidly. Interfacial properties of a nanostructures material could, therefore, enable new functional devices. In this regard, self-assembled mesoporous silica (MS) is attractive for its extremely large internal surface area and controllable nanoporous structure [30]. Recently, we showed that enhanced blue photoluminescence (PL) in three-dimensional Si nanocrystals embedded in MS had been reported [24].

In this thesis, we demonstrate a high response diode-like UV-NIR detector with a capping layer of nc-Si-embedded MS. This new technology is easy and fully compatible with the IC industry on synthesizing dense, uniform, size-tunable Si NCs within mesoporous silica film as efficient far short-wavelength sensing layers. Gain in this photodiodes was found and attributed to an enhancement of reverse bias of positive voltage by the formation of positively charged capped layer due to photoionization of electrons.

1.3 Reference

1. T. Takimoto, N. Fukunaga, M. Kubo, and N. Okabayashi, *IEEE Trans. Consumer Electronics*, **4**, 137 (1998).
2. Y. Mai, S. Klein, X. Geng, and F. Finger, *Appl. Phys. Lett.* **85**, 2839 (2004).
3. H. Ouyang, C. C. Striemer, and P. M. Fauchet, *Appl. Phys. Lett.* **88**, 163108 (2006).
4. F. Gan, L. Hou, G. Wang, H. Liu, and J. Li, *Materials Science and Engineering: B* **76**, 63 (2000).
5. M. V. Wolkin, J. Jorne, P. M. Fauchet, G. Allan, and C. Delerue, *Phys. Rev. Lett.* **82**, 197 (1999).
6. G. Allan, C. Delerue, and M. Lannoo, *Phys. Rev. Lett.* **76**, 2961 (1996).
7. M. H. Nayfeh, N. Rigakis, and Z. Yamani, *Phys. Rev. B* **56**, 2079 (1997).
8. O. M. Nayfeh, S. Rao, A. Smith, J. Therrien, and M. H. Nayfeh, *IEEE Photon. Technol. Lett.* **16**, 1927 (2004).
9. Munir H. Nayfeh, Satish Rao, Osama Munir Nayfeh, Adam Smith, and Joel Therrien, *IEEE Transactions on Nanotechnology*, **4**, 660 (2005).
10. J. P. Zheng, K. L. Jiao, W. P. Shen, W. A. Anderson, and H. S. Kwok, *Appl. Phys. Lett.* **61**, 459 (1992).
11. M. K. Lee, C. H. Chu, Y. H. Wang, S. M. Sze, *Optics Letters*, **26**, 160 (2001).
12. M. El kurdi, P. Boucaud, a) S. Sauvage, and G. Fishman *JAP*, 92, 1858 (2002)
13. C.-H. Lin, C.-Y. Yu, P.-S. Kuo, C.-C. Chang, T.-H. Guo, C.W. Liu *Thin Solid Films*, 508, 389 (2006)
14. S. J. Chang, a, z C. L. Yu, a P. C. Chang, b and Y. C. Lina *Electrochemical and Solid-State Letters*, 10. H196- H198 (2007)

15. Xiaping Chen, Weifeng Yang, Zhengyun Wu *Microelectronic Engineering* **83** (2006)
16. L. T. Canham, *Appl. Phys. Lett.* **57**, 1046 (1990).
17. N. Koshida, X. Sheng, and T. Komoda, *Appl. Surf. Sci.* **146**, 371 (1999).
18. C. M. Yang, A. T. Cho, F. M. Pan, T. G. Tsai, and K. J. Chao, *Adv. Mater.* **13**, 1099 (2001).
19. Y. D. Glinka, S. H. Lin, L. P. Hwang, and Y. T. Chen, *Appl. Phys. Lett.* **77**, 3968 (2000).
20. L. Pavesi, L. Dal Negro, C. Mazzoleni, G. Franzo, and F. Priolo, *Nature*, **408**, 440 (2000).
21. J. Y. Zhang, X. M. Bao, Y. H. Ye, and X. L. Tan, *Appl. Phys. Lett.* **73**, 1790 (1998).
28. D. P. Yu, Q. L. Hang, Y. Ding, H. Z. Zhang, Z. G. Bai, J. J. Wang, Y. H. Zou, W. Qian, G. C. Xiong, and S. Q. Feng, *Appl. Phys. Lett.* **73**, 3076 (1998).
22. M. S. El-Shall, S. Li, T. Turkki, D. Graiver, U. C. Pernisz, and M. I. Baraton, *J. Phys. Chem.* **99**, 17806 (1995).
23. D. Y. Zhao, P. D. Yang, N. Melosh, J. G. Feng, B. F. Chmelka, and G. D. Stucky, *Adv. Mater.* **10**, 1380 (1998).
24. A. T. Cho, J. M. Shieh, J. Shieh, Y. F. Lai, B. T. Dai, F. M. Pan, H. C. Ku, Y. C. Lin, K. J. Chao, and P. H. Liu, *Electrochem. Solid-State Lett.* **8**, G143 (2005).

Chapter 2 Basic Theory About Photodetector

2.1 Schottky contact

The ideal energy diagram for a particular metal and n-type semiconductor before marking contact is shown in Fig.2.1. The vacuum level is a reference level. The parameter ϕ_m is the metal work function (measured in volts), ϕ_s is the semiconductor work function, and χ is known as the electron affinity. We have assumed that $\phi_m > \phi_s$. Before contact, the Fermi level in the semiconductor was above that in the metal. In order for the Fermi level to become a constant through the system in the thermal equilibrium, electrons from the semiconductor flow into the lower energy states in the metal. Positively charged donor atoms remain in the semiconductor, creating a space charge region. [1]

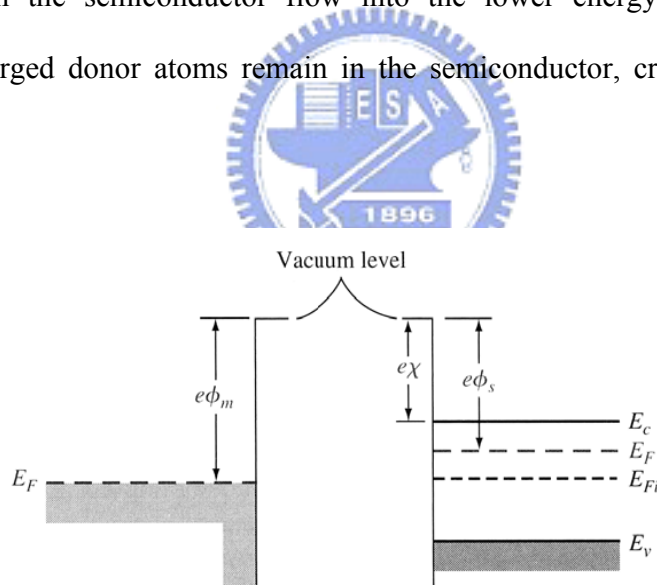


Fig. 2.1 Energy-band diagram of a metal and semiconductor before contact

After contact, the ideal energy-band diagram of a metal-n -semiconductor junction for $\phi_m > \phi_s$ is shown in Fig.2.2. The parameter ϕ_{BO} is the ideal barrier height of the semiconductor contact, the potential barrier seen by electrons in the metal trying to move into the semiconductor.

The barrier is known as the Schottky barrier and is given, ideally, by

$$\phi_{BO} = (\phi_m - \chi) \quad (2.1)$$

On the semiconductor side, V_{bi} is the built-in potential barrier. The barrier, similar to the case of the pn junction, is the barrier seen by electrons in the conduction band trying to move into the metal. The built-in potential barrier is given by

$$V_{bi} = \phi_{BO} - \phi_n \quad (2.2)$$

which make a slight function of the semiconductor doping, as was the case in a pn junction.[1-2]

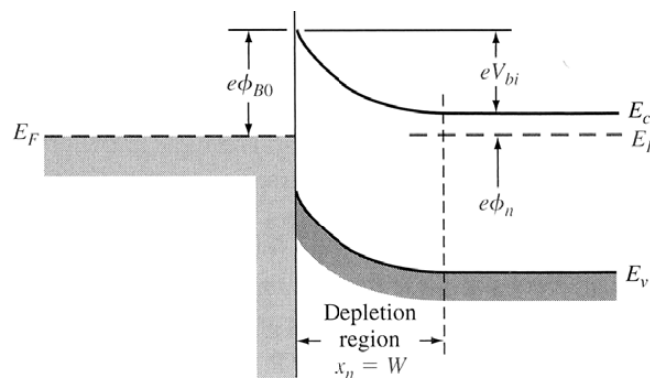
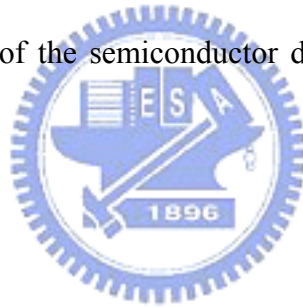


Fig. 2.2 Ideal energy-band diagram of a metal- semiconductor junction for $\Phi_m > \Phi_s$

2.2 Schottky barrier photodiodes

Schottky barrier photodiodes have been studied quite extensively and have also found application as ultraviolet detectors [3]. These devices reveal some advantages over p-n junction photodiodes: absence of high-temperature diffusion processes, fabrication simplicity, and high speed of response.

The current transport processes

The interface will form a barrier after particular metal and semiconductor making contact. This contact is a rectifying contact and is called for Schottky contact. On the other hand, Ohmic contacts are not rectifying contacts and low-resistance junction providing conduction in both directions between the metal and semiconductor. The current transport in a metal-semiconductor junction is due mainly to majority carriers as opposed to minority carriers in a pn junction. The current can be transported in various ways under forward bias conditions as shown in Fig. 2.1. The four processes are: (1) Emission of electrons from the semiconductor over the top of the barrier into the metal, (2) tunneling through the barrier, (3) generation-recombination, (4) Recombination in the neutral region [4]

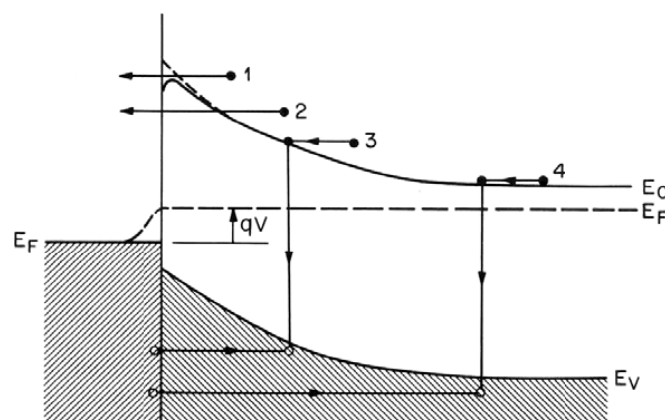


Fig. 2.3 The mechanisms of current transport in forward-biased Schottky contact

There are various theories to describe the mechanism of electrons going through potential barrier. These mechanisms include diffusion, thermionic emission, and unified thermionic emission diffusion. It is now widely accepted that, for high-mobility semiconductors with impurity concentrations of practical interest, the thermionic emission theory appears to explain qualitatively the experimentally observed $I-V$ characteristics.

The thermionic emission characteristics are derived by using the assumptions that the barrier height is much larger than kT , so that the Maxwell-Boltzmann approximation applies and that thermal equilibrium is not affected by this process. Fig. 2.4 shows the one-dimensional barrier with an applied forward-bias voltage V_a and shows two electron current density components. The current $J_{s \rightarrow m}$ is the electron current due to the flow of electron from the semiconductor into the metal, and the current $J_{m \rightarrow s}$ is the electron current density due to the flow of electrons from the metal into semiconductor. The conventional current direction is opposite to the electron flow. The net current density in the metal-to-semiconductor junction can be written as:

$$J = J_{s \rightarrow m} - J_{m \rightarrow s} \quad (2.3)$$

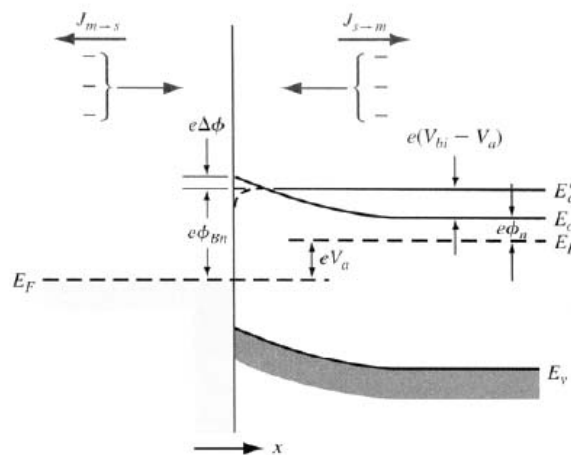


Fig. 2.4 Energy-band diagram of a forward-biased metal-semiconductor junction including the image lowering effect.

which is defined to be positive in the direction from the metal to the semiconductor.

We find that

$$J = \left[A^* T^2 \exp\left(\frac{-e\phi_{Bn}}{kT}\right) \right] \left[\exp\left(\frac{eV_a}{kT}\right) - 1 \right] \quad (2.4)$$

where

$$A = \frac{4\pi e k^2 m^*}{h^3} \quad (2.5)$$

The parameter A^* is called the effective Richardson constant. Equation (2.4) can be written in the usual diode form as

$$J = J_{st} \left[\exp\left(\frac{eV_a}{kT}\right) - 1 \right] \quad (2.6)$$

where J_{st} is the reverse-saturation current density and is given by

$$J_{st} = A^* T^2 \exp\left(\frac{-e\phi_{Bn}}{kT}\right) \quad (2.7)$$

The equation is similar to the transport equation for p-n junctions. However, the expression for the saturation current densities is quite different.

2.3 Quantum Efficiency

External quantum efficiency η ($0 \leq \eta \leq 1$) of a photodetector is the number of photoelectrons generated per incident photon that contributes to the detector current. When many photons are incident, η is the ratio of the flux of generated electron-hole pairs that contribute to the detector current to the flux of incident photons [4,5]. The higher quantum efficiency the more electrons will be generated by incident photons. The quantum Efficiency is defined as

$$\eta = (1 - R)\zeta[1 - \exp(-\alpha d)] \quad (2.8)$$

where R is the optical power reflectance at the surface, The first factor $(1-R)$ represents the effect of reflection at the surface of the device. ζ is the fraction of electron-hole pairs that successfully avoid recombination at the material surface and contribute to the useful photocurrent, α the absorption coefficient of the material (cm^{-1}), and d the photodetector depth. $[1 - \exp(-\alpha d)]$ is the fraction of the photon flux absorbed in the bulk of the material. The device should have a sufficiently large value of d to maximize this factor.

2.4 Responsivity

The definition of photodetector's responsivity is the ratio of incident light power to induced photocurrent. the responsivity can be represented as

$$I_{photo} = RP_{opt} = \eta e \Phi = \frac{\eta e P_{opt}}{h\nu} \quad (2.9)$$

where I_{photo} is the photocurrent, and Φ is the photon flux. If every photon were to generate a single photoelectron ($\eta = 1$), a photon flux would produce an electron flux, and then $I_{photo} = e \Phi$. A photon at frequency ν has energy $h\nu$. Thus optical power $P_{opt} = h\nu \Phi$ (watt), and $I_{photo} = e P_{opt} / h\nu$. The responsivity R of device has units of A/W and is given by

$$R = \frac{I_{photo}}{P_{opt}} = \frac{\eta e}{h\nu} = \eta \frac{\lambda_0}{1.24} \quad (\text{A/W}) \quad \lambda_0 \text{ in } \mu\text{m} \quad (2.10)$$

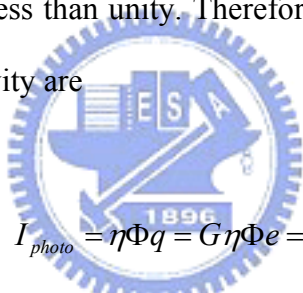
where λ_0 is the wavelength of incident light. We can see that R increases with λ_0 (under constant power) because photoelectric detectors are responsive to the photon flux rather than to the optical power. As λ_0 increases, a given optical power is carried by more photons, which, in turn, produce more electrons. Since the wavelength dependence of η comes into play for both long and short wavelengths, the region over which R increases with λ_0 is limited.

2.5 Gain effect

The formulas presented above are predicated on the assumption that each carrier produces a charge e in the detector circuit. However, many devices produce a charge q in the circuit that differs from e [5]. Such devices are said to exhibit gain. The gain G is the average number of circuit electrons generated per photocurrent pair. G should be distinguished from η , which is the probability that an incident photon produces a detectable photocurrent pair. The gain, which is defined as

$$G = \frac{q}{e} \quad (2.11)$$

can be either greater than or less than unity. Therefore, more general expressions for the photocurrent and responsivity are



$$I_{photo} = \eta \Phi q = G \eta \Phi e = \frac{G \eta e P}{h\nu} \quad (2.12)$$

and

$$R = \frac{G \eta e}{h\nu} = G \eta \frac{\lambda_0}{1.24} \quad \lambda_0 \text{ in } \mu\text{m} \quad (2.13)$$

respectively.

The responsivity of a photoconductor is given by (2.13). The device exhibits an internal gain which, simply viewed, comes about because the recombination lifetime and transit time generally differ. Suppose that electrons travel faster than holes and that the recombination lifetime is very long. As the electron and hole are transported to opposite sides of the photoconductor, the electron completes its trip sooner than the hole. The requirement of current continuity forces the external circuit to provide another electron immediately, which enters the device from the wire at the left. This

new electron moves quickly toward the right, again completing its trip before the hole reaches the left edge. This process continues until the electron recombines with the hole. A single photon absorption can therefore result in an electron passing through the external circuit many times. The expected number of trips that the electron makes before the process terminates is [7]

$$G = \frac{\tau}{\tau_e} \quad (2.14)$$

Where τ is the excess-carrier recombination lifetime and τ_e is the electron transit time across the sample. The charge delivered to the circuit by a single electron-hole pair in this case is $q = G e > e$ so that the device exhibits gain.

2.6 Detectivity

The specific detectivity D^* is used to characterize performance of a photodetector. A more-sensitive detector has a larger detectivity than a less-sensitive detector. The definition of D^* is

$$D^* = \frac{e\eta}{h\nu} \sqrt{\frac{R_0 A}{4kT}} \quad (2.15)$$

where e is the electronic charge, η is the quantum efficiency, h is Planck's constant, ν is the frequency of the radiation, R_0 is the dynamic resistance at zero bias, A is the detector area, k is Boltzman's constant, and T is the absolute temperature [6]. The advantage of D^* as a figure of merit is that it is normalized to an active detector area of 1cm^2 and noise bandwidth of 1Hz. Therefore, D^* may be used to compared directly the merit of detectors of different size whose performance was measured using different bandwidths.

2.7 C-V measurement

Capacitance-Voltage (C-V) Measurement is one of the very basic measurements that can be done to characterize semiconductor devices. What is normally done is the device is hooked up to the instrument and C-V graphs are plotted and with that data we can conclude the type of device, whether it's a *p*-type or an *n*-type device and many other parameters. The main aim of the C-V measurement is to extract the doping information of the diode.

The capacitance of a device is defined as

$$C = \frac{dQ}{dV} \quad (2.15)$$

where dQ is the magnitude of the differential charge in charge on one plate as a function of the differential change in voltage dV across the capacitor. For a MOS capacitor, there are three operating conditions: accumulation, depletion, and inversion.

Fig. 2.5 (a) shows the energy-band diagram of an MOS capacitor with a *p*-type substrate for the case when a negative voltage is applied to the gate. A small differential change in voltage across the MOS structure will cause a differential change in charge on the metal gate and also in the hole accumulation charge, as shown in **Fig 2.5 (b)**, the capacitance C per unit area of the MOS capacitor for this accumulation mode just the oxide capacitance

$$C_{acc} = C_{ox} = \frac{\epsilon_{ox}}{t_{ox}} \quad (2.16)$$

where C_{ox} is the oxide capacitance per unit area, and ϵ_{ox} , t_{ox} are the permittivity and thickness of oxide, respectively.

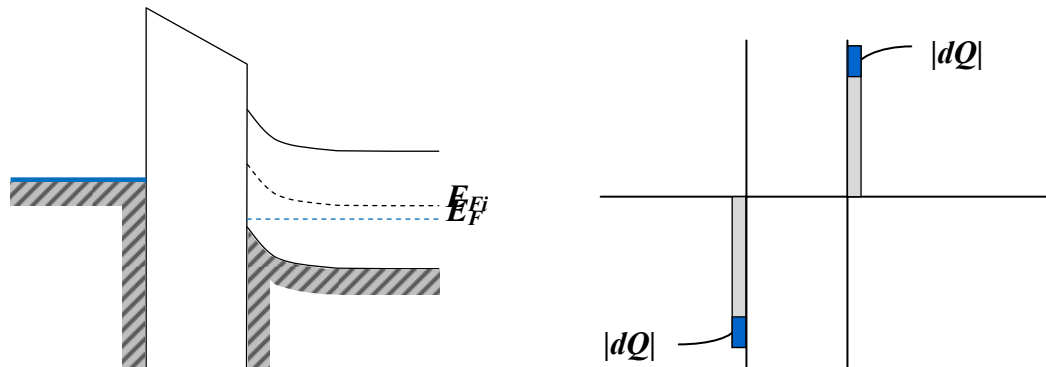


Fig. 2.5 (a) Energy-band diagram through an MOS capacitor for the accumulation mode. (b) Differential charge distribution at accumulation for a differential change in gate voltage.

In inversion condition, a positive voltage is applied to the gate, inducing a space charge region in the semiconductor. In the limit of very high frequency, the inversion layer charge will not respond to a differential charge in capacitor voltage. **Fig 2.6(a)** shows the energy-band diagram of the MOS device for this condition. **Fig 2.6(b)** illustrate the charge distribution through the device. A small differential change in voltage across the capacitor will cause a differential change in the space charge width. The total capacitance of the series combination is

$$\frac{1}{C_{inv}} = \frac{1}{C_{ox}} + \frac{1}{C_s} \quad (2.17)$$

$$C_{inv} = \frac{C_{ox} \cdot C_s}{C_{ox} + C_s} \quad (2.18)$$

Where C_s is the capacitance of semiconductor in the space charge width, and C_{inv} is the total capacitance in inversion condition.

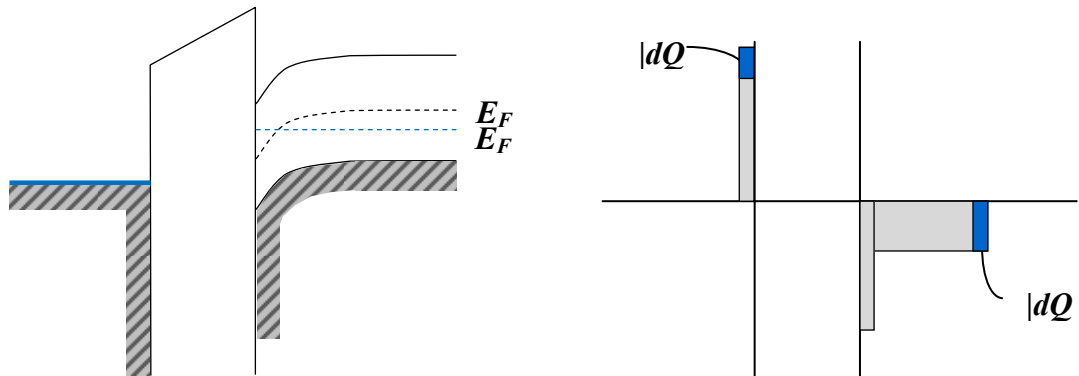


Fig 2.6 (a) Energy-band diagram through an MOS capacitor for the inversion mode.(b) Differential charge distribution at inversion for a differential change in gate voltage.(high frequency)

The flat-band voltage is defined as the applied gate voltage such that there is no band bending in the semiconductor. It was given by

$$V_{FB} = \phi_{ms} - \frac{Q_{ss}}{C_{ox}} \quad (2.19)$$

Where Q_{ss} is the equivalent fixed oxide charge and ϕ_{ms} is the metal-semiconductor work function difference. The flat-band voltage shift to more negative voltages for a positive fixed oxide charge. Since the oxide charge is not a function of gate voltage, the curves show a parallel shift with oxide charge, and the shape of the C-V curves remains the same as the ideal characteristics.

The C-V characteristics can be used to determine the equivalent fixed oxide charge. Using the equation given in **Ref. 7**, for a given MOS structure, C_{ox} are given, ΔV_{FB} can be determined.

$$\Delta V_{FB} = \frac{1}{\epsilon} \int_0^{x_0} x \cdot \rho(x) dx \quad (2.20)$$

Where ϵ is the permittivities [7]. In the case of multilevel charge storage,

$$\Delta V_{FB} = \frac{e \cdot n_{dot}}{\epsilon_{ox}} \left(t_1 + \frac{\epsilon_{ox}}{2\epsilon_{si}} t_{dot} \cdot N + t_2 + t_3 + \dots \right) \quad (2.21)$$

Where t_n is the upper control gate oxide thickness, t_{dot} is the nanocrystal diameter, and ϵ_{ox} and ϵ_{si} are the permittivities of the oxide and silicon, respectively[7].

2.8 Reference

1. Donald A. Neamen, Semiconductor Physics & Devices, third Edition.
2. S.M. Sze, Physics of semiconductor devices. New York: John Wiley & Sons 1981.
3. David Wood, "Optoelectronic Semiconductor Devices", (Prentice Hall, New York, 1994).
4. M. Razeghi and A. Rogalski, J. Appl. Phys. 79, 7433 (1996).
5. Bahaa E. A. Saleh and Malvin Carl Teich, "Fundamentals of Photonics", (Wiley - Interscience Publication, New York, 1991).
6. C. K. Wang, T. K. Ko, C. S. Chang, S. J. Chang, Y. K. Su, T. C. Wen, C. H. Kuo, and Y. Z. Chiou, IEEE Photon. Technol. Lett. **17**, 2161 (2005).
7. T. Z. Lu, a M. Alexe, R. Scholz, V. Talelaev, and M. Zacharias, APL **.87**, 202110 (2005)

Chapter 3 Experimental Details

3.1 Process

3.1.1 Preparation of mesoporous silica template

The mesoporous silica (MS) films [1] are initially spin-coated on silicon wafers using sol-gel-prepared precursors that contain different organic templates (cetyltrimethylammonium bromide (CTAB), polyoxyethylene cetyl ether (Brij-56), and Triblock copolymer Pluronic P-123 (P123)) for controlling the pore-size, followed by drying at 40°C and baking at 110°C for five and three hours respectively. The MS film was formed by molecular self-assembly aggregation in this step. The film was employed as nanotemplate for the growth of three-dimensional array of Si (Ge) nanocrystals (nc). The flowchart of mesoporous silica nanotemplate films preparing is shown in **Fig. 3.1**.

The sol-gel was made by mixing H₂O, HCl, tetraethylorthosilicate (TEOS), and ethanol at 70°C for 90 min. The molar ratios of reactants were 1:0.008-0.03:3.5-5:0.003-0.03:10-34(TEOS/(P123,CTAB,Brij-56)/H₂O/HCl/ethanol).

After aged at room temperature for more than 3 hours, it was spin-coated onto silicon substrates at 2200 rpm for 30 seconds.

MS template preparing flowchart

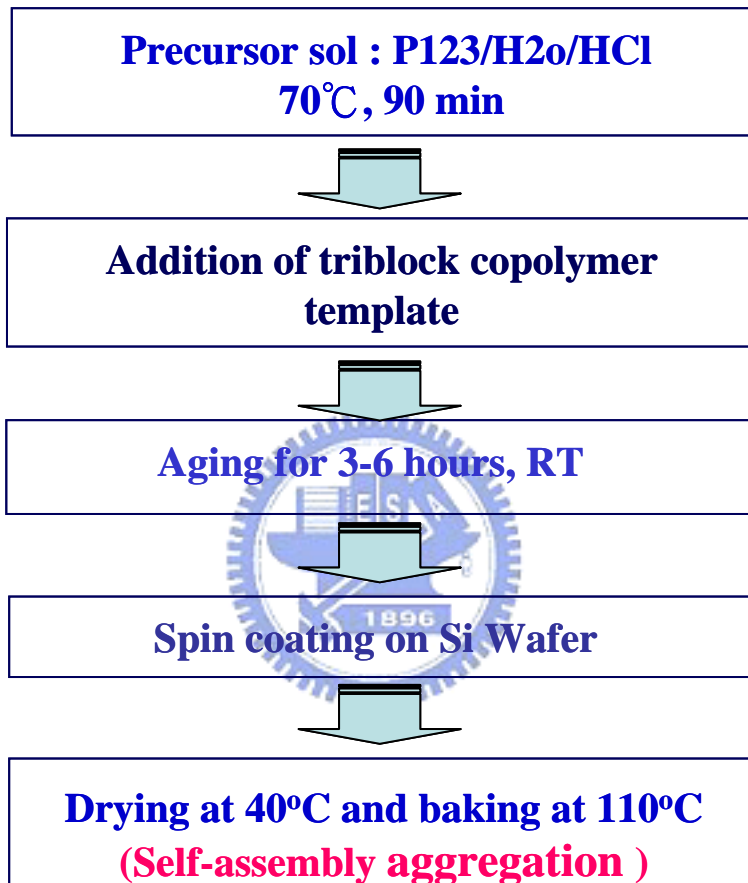


Fig. 3.1 Flowchart of sol-gel procedure for preparing mesoporous silica nanotemplate films.

3.1.2 The growth of 3-D Si (and Ge) nanocrystals by HDP-CVD

Inductivity coupled plasma-chemical vapor deposition (ICPCVD) [2,3] of thin films is widely used in microelectronic circuit manufacturing. Materials deposited include conductors such as tungsten, copper, aluminum, transition-metal silicides, and semiconductors such as gallium arsenide, epitaxial and polycrystalline silicon, and dielectrics such as silicon oxide, silicon nitride, and silicon oxynitride. High-Density Plasma Chemical Vapor Deposition (HDPCVD) with the features of low process temperature, low pressure and high plasma density was chosen to growth Nc-Si (or nc-Ge) in the MS template.

Base pressure of chamber was as low as 10^{-6} Torr. Mixture plasma at 500W was powered on after loading MS-coated wafers into the chamber. During the entire process, pressure was kept below 10m torr and the substrate temperature was hold at 400°C . MS films embedded with high density silicon (or germanium) nanocrystals were prepared by using 12 – 18 cycles of pulsed $\text{SiH}_4 + \text{H}_2 / \text{H}_2$ (or $\text{GeH}_4 + \text{H}_2 / \text{H}_2$) ICP with a duty cycle of 1 second/ 3 seconds.

There are numerous reactions involved in the formation of nc-Si (or nc-Ge) in the MS template with ICPCVD . Firstly, the pure- H_2 -ICP-plasma (step A of Fig. 3.2) removes organic-templates of MS matrices lightly for enabling limited nucleation sites of Si-OH on pure-surfaces [4]. This is a self-limiting reaction (SLR), which is a core concept in atomic layer deposition [5]. Sequentially, ICP-dissolved SiH_x (GeH_x) species (step B of Fig. 3.2) in the form of nanoclusters diffuse into the nanopores, and are then absorbed and embedded in the residual organic-template of MS. They eventually react with the nucleation sites through hydrogen-elimination reaction (HER). Therefore, both

self-limiting reaction [5] and hydrogen-elimination reaction (HER) [4,5] govern the conversion of ICP-dissolved species in MS into nc-Si (or nc-Ge). The density of nc-Si (or nc-Ge) grown by pulsed plasma can as high as $2.5 \times 10^{18} \text{ /cm}^3$.

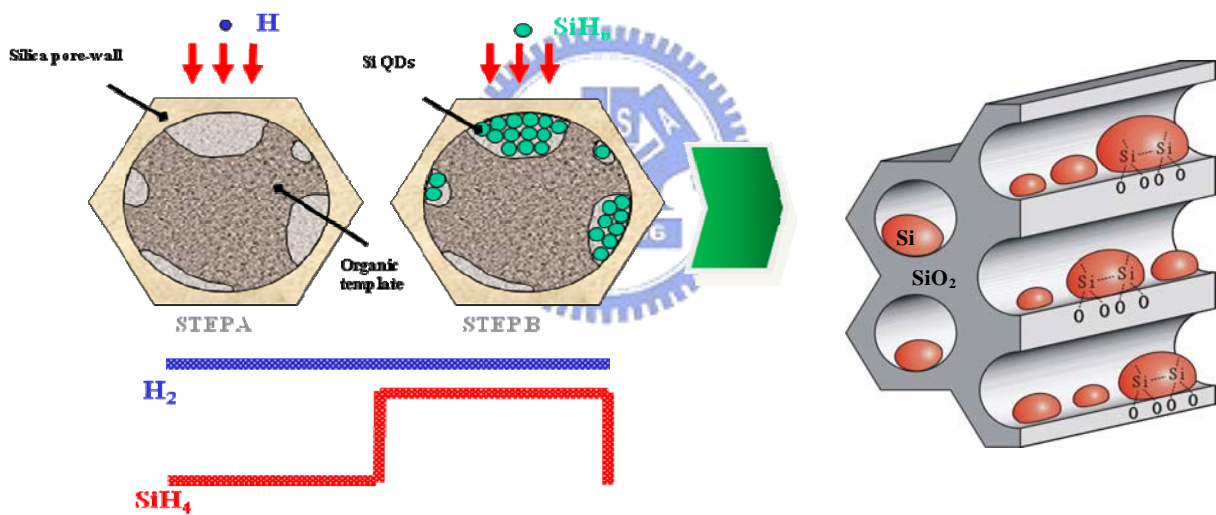


Fig. 3.2 Schematic mechanism of 3D Si nanodots formed by pulse ICP process.

3.1.3 Device fabrication

The device structure is depicted schematically in Fig. 1. First, a 220-nm-thick MS template layer is formed on Si substrates. Si nanocrystals were thereafter synthesized in the MS templates by using a plasma deposition process.¹² For device applications, the organic contents of MS are removed by calcinations in the same chamber with H₂ plasma at the flow rate of 150 sccm for 2 hours. The indium–tin–oxide (ITO) films of 2400 Å^o thick were deposited onto the samples by E-gun evaporation, followed by 20 min of annealing at 400°C in N₂ ambient.

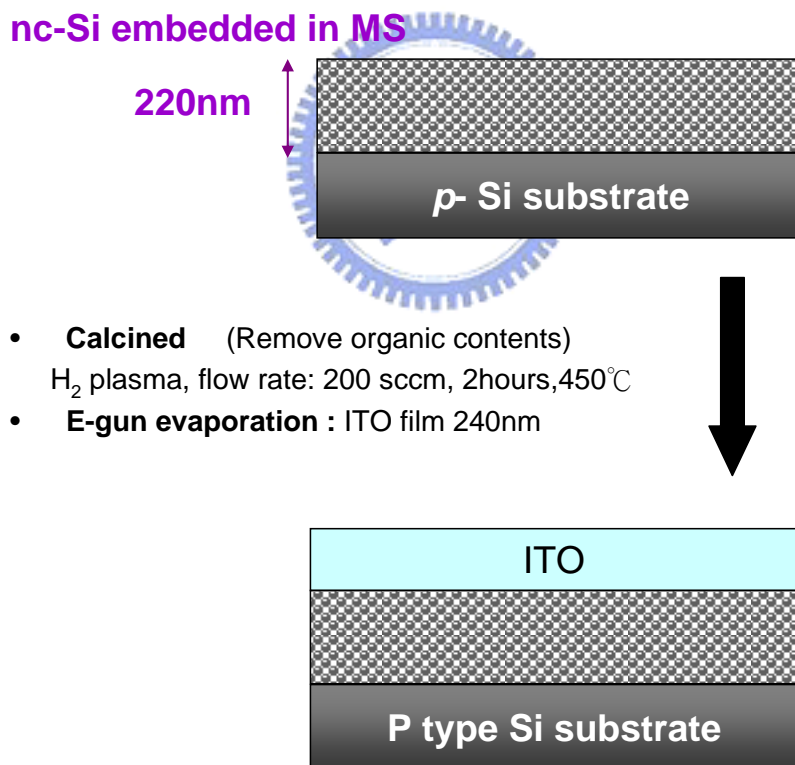


Fig. 3.3 A schematic drawing illustrating the configuration of the photodiodes of ITO/nc-Si embedded MS /p-Si.

3.2 Experiment Setup

3.2.1 The Capacitance-Voltage measurement system

The system we used to measure the low frequency capacitance is **Bias Temperature Stress measurement system (BTS)**: Keithley 590 CV analyzer · Keithley 595 Quasistatic CV meter · Keithley 230 programmable voltage source · Keithley 5951 remote input coupler and computer with AIT software installed. **Fig 3.4** shows the schematic diagram of C-V measurement system.

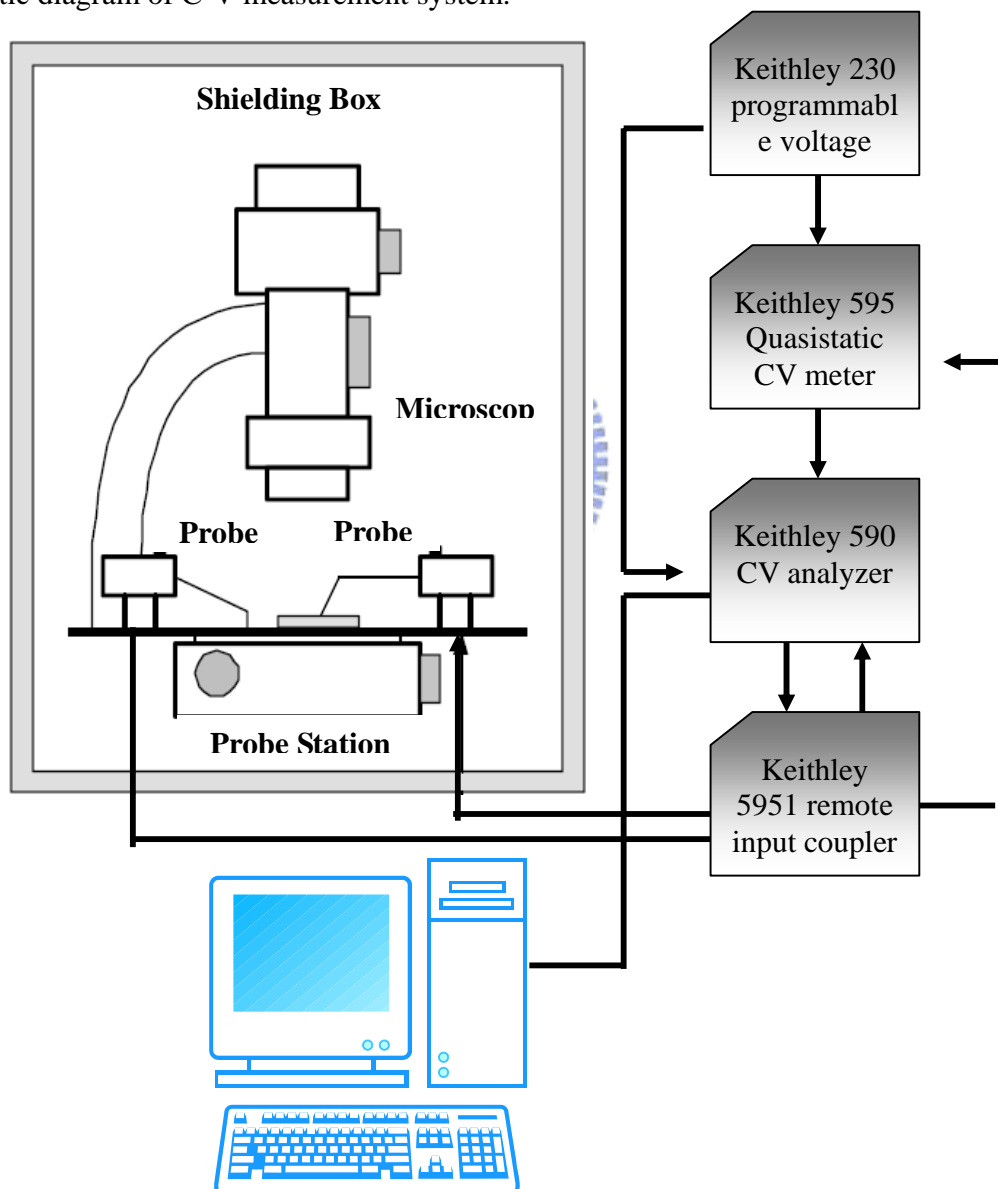


Fig. 3.4 The schematic diagram of C-V measurement system.

3.2.2 Spectral responsivity measurement system

The setup of spectral responsivity measurement system as showed in Fig. 3.5. Spectral responsivity measurements were achieved using a 300 W xenon lamp with wavelength selection using a double-grating monochromator (Jobin-Yvon Gemini 180). Lamp focuses on the sample through 2 focal lens which focal length is five centimeter. The spot size is about $3 \times 4 \text{ mm}^2$ after focusing and the power is $0.1 \sim 0.7 \text{ mW}$ on the surface of the sample. The measurements of current-voltage characteristics were controlled by the Labview programs. A Keithley 2400 source measurement unit was used to apply biases to the electrodes., Bias-dependent responsivity was measured in dc mode by recording current–voltage ($I - V$) curves under a fixed wavelength and power. The power density of the excitation was determined with a calibrated UV Si photodetector.

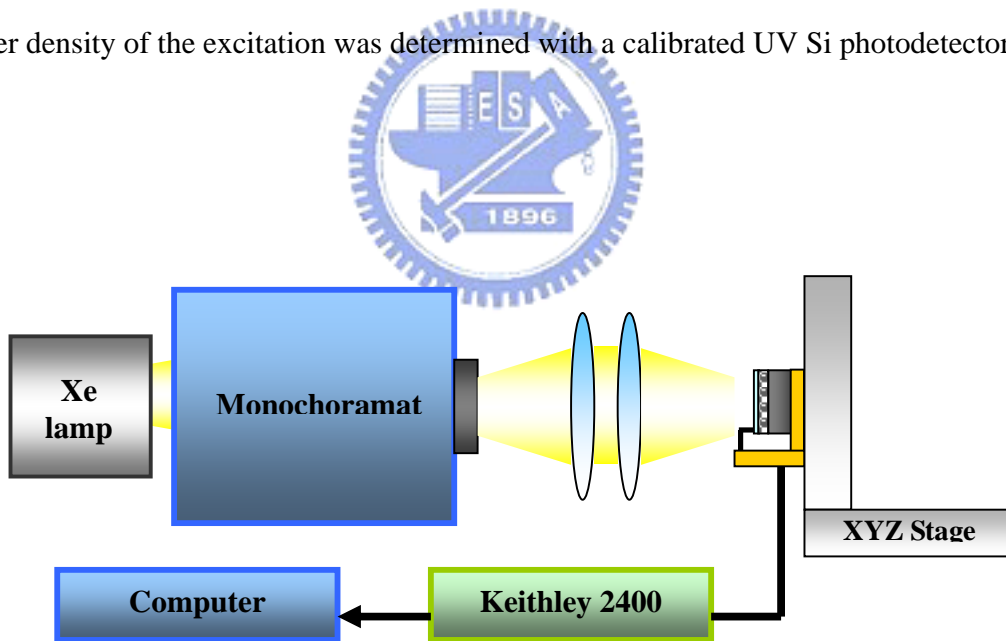


Fig. 3.5 Diagram of spectral responsivity measurement system.

3.3 References

1. D. Zhao, P. Yang, N. Melosh, J. Feng, B. F. Chmelka, and G. D. Stucky, *Adv. Mater.* **10**, 1380 (1998).
2. J. M. Shieh, K. C. Tsai, and B. T. Dai, *Appl. Phys. Lett.* **81**, 1294 (2002).
3. J. H. Wu, J. M. Shieh, B. T. Dai, and Y. S. Wu, *Electrochemical and Solid-State Letters* **7 (6)**, G128 (2004).
4. Ö. Dag, G. A. Ozin, H. Yang, C. Reber, and G. Bussière, *Adv. Mater.* **11**, 474 (1999).
5. Y. J. Lee, and S. W. Kang, *Electrochemical and Solid-State Letters*, **6 (5)**, C70 (2003).



Chapter 4 Results and Discussions

4.1 TEM Image

The experiment was started with the formation of a 220-nm-thick MS template layer on *p*-type silicon substrates. Si or Ge nanocrystals were thereafter synthesized in the MS templates by using a plasma technique [1]. **Fig. 4.1** is the cross-sectional transmission electron microscopy (TEM) image for the sample. One can see that the MS film was decorated with $\sim 10^{18} \text{ cm}^{-3}$ of Si nanocrystals, and the mean size of nc-Si was found to be 4 nm.

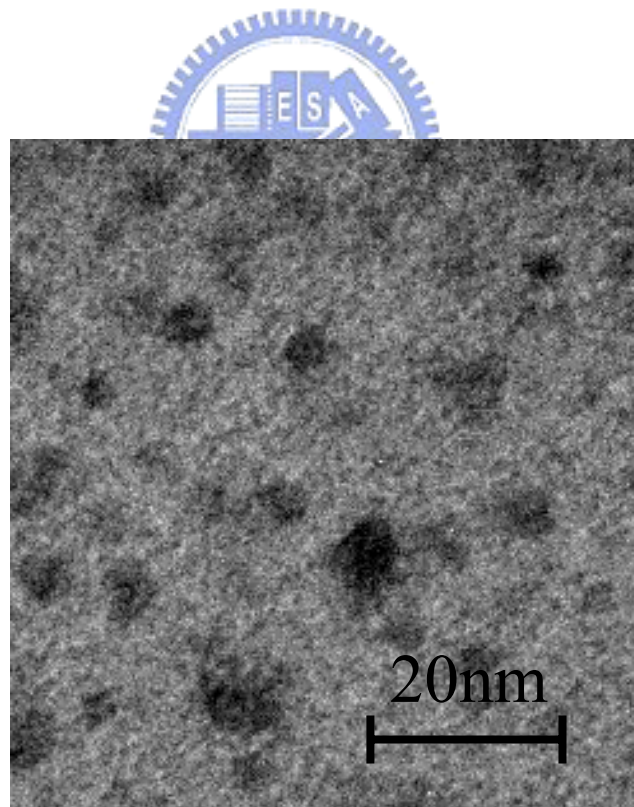


Fig. 4.1 The cross-sectional TEM images of the mesoporous silica (MS) films with high density silicon nanocrystals.

4.2 C-V Measurement

For C-V measurement, a compound oxide with structure of SiO₂/MS with Si (Ge) QD imbedded/SiO₂ was formed on *p*-type Si wafer. The tapping oxide and tunneling oxide with thickness of 10nm and 5nm were deposited by HDPCVD, with gas flow of SiH₄:N₂O=1:15 sccm and process temperature of 375⁰C. After that, the top and back contact layers of Aluminum were plated by thermal coater. **Fig 4.2 (a)** illustrates the device structure, and **(b)** is the image of device.

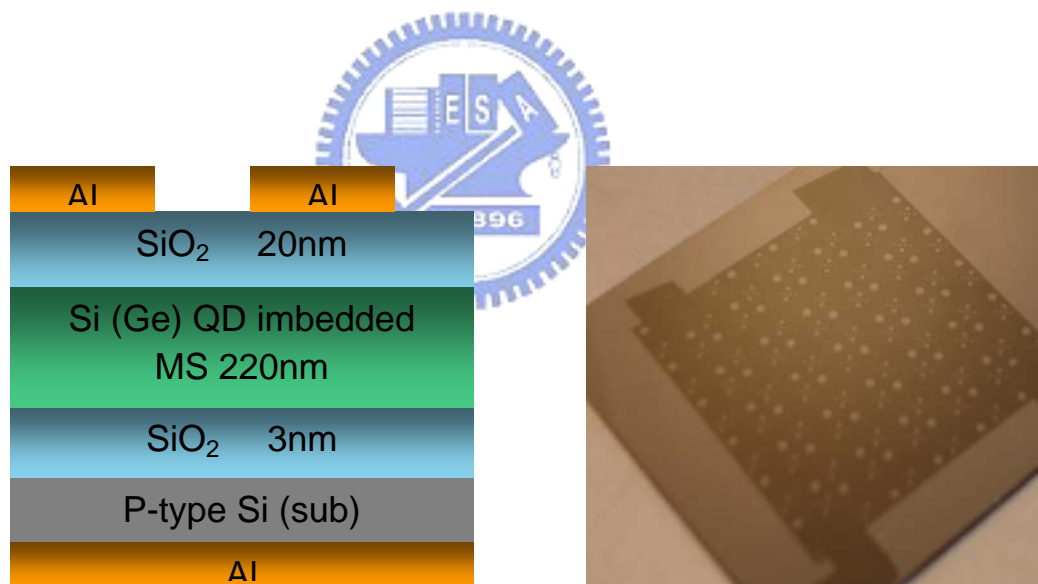


Fig. 4.2 (a) A schematic drawing illustrate the configuration of the device with compound oxide. **(b)** The image shows device with Al contact layer.

To investigate the trapping characteristics of the structure we performed multiple up-down capacitance voltage (C - V) sweeps between inversion and accumulation regions. The measurements were performed at 1MHz using BTS C - V measurement system at room temperature. **Fig 4.3(a)** and **(b)** illustrate the characteristic multilevel charge storage for our metal-oxide-semiconductor (MOS) structures. The C - V hysteresis was observed, which is caused by the successive charge trapping and de-trapping processes in the Si (Ge) NCs. With sweeping range of 20V, the hysteresis widths of Si and Ge doped sample can be as large as 16 and 12 V, respectively.

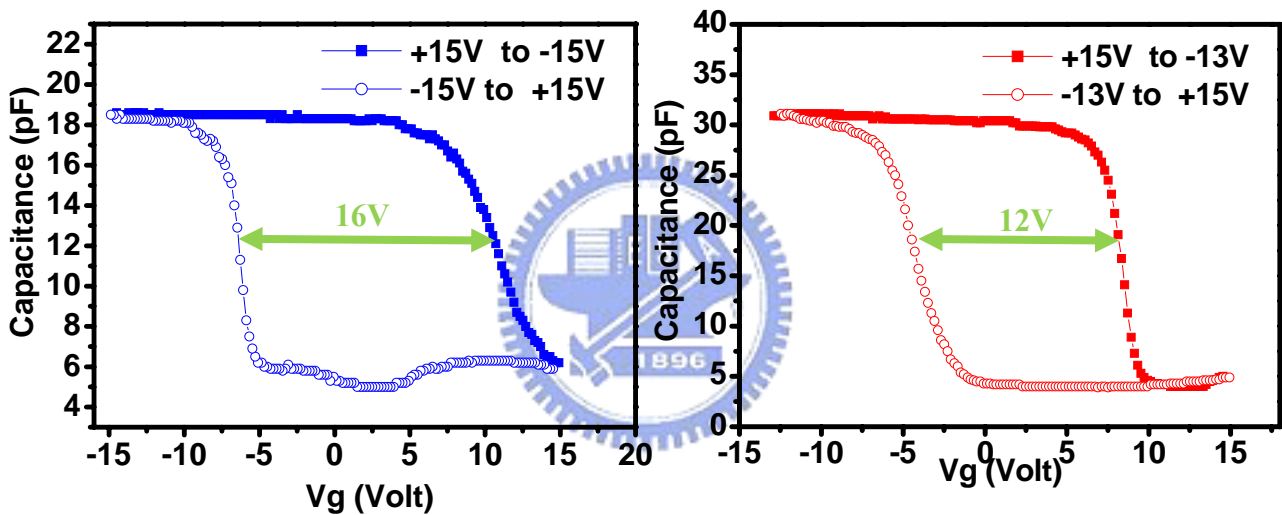


Fig. 4.3 High frequency C - V characteristics of the sample (a) with Si QD and (b) Ge QD imbedded in MS.

As can be seen in **Fig 4.4**, a different programming bias applied at the gate results in a various C - V hysteresis widths. Hence, the narrowest C - V loop corresponds to the charging of only one layer and the widest one to the charging of more layers of QDs imbedded in MS. The sweep is from the inversion to the accumulation region for the MOS devices based on p -type substrates. For negative program bias, more and more holes are trapped in the QDs which are evident by the counterclockwise

hysteresis. After each sweep, holes charged in the QDs were always erased by positive bias to bring the device back to the neutral stage.

Fig 4.4 shows characteristic of multilevel charge storage, the steps in the flat-band shift, was caused by the charging of the numerous layers of nc-Ge.

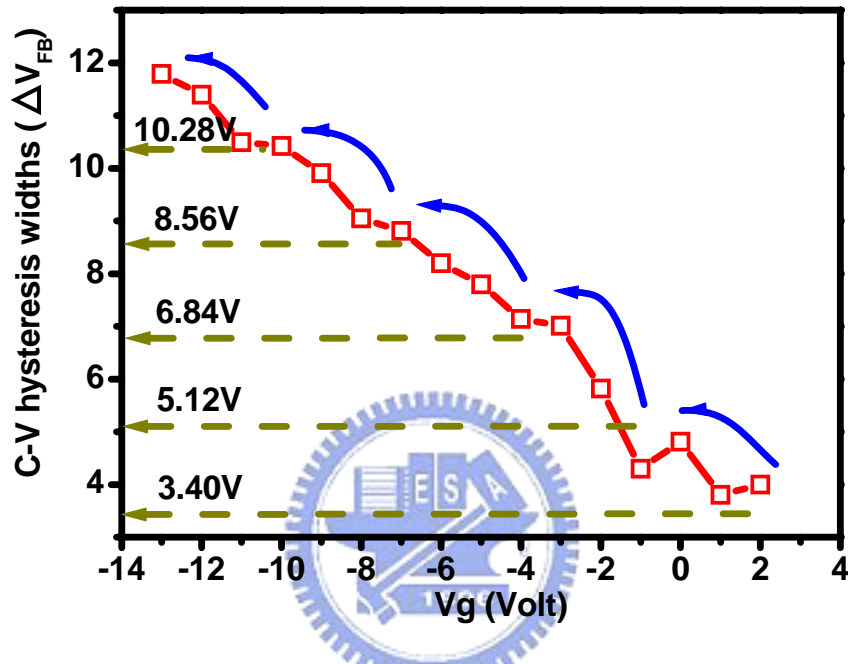


Fig 4.4 The dependence of the memory window, i.e., the flatband shift on programming voltage. There are multilevel charge storages in mesoporous silica matrix with Ge nanocrystals.

We calculated the flatband voltage using the equation (2.21)[2]. Set ΔV_{FB} equal to 12 V, the diameter of nc-Ge to 4nm. There would be 6 layers of nc-Ge distributed in the oxide layer, and the density of nc-Ge per layer would be $9.4 \times 10^{12} \text{ cm}^{-2}$ ($\sim 10^{18} \text{ cm}^{-3}$ per unit volume), very close to the value we got from TEM image. The shift of flatband voltage caused by charging of numerous layers of nc-Ge layers (using equation (2.21)) coincided with the multilevel charge storage character shown in **Fig 4.4**.

4.3 I-V characteristics of the photodetector

For light detection, a 220-nm-thick MS template layer is formed on *p*-type Si substrates. Si nanocrystals were thereafter synthesized in the MS templates by using a plasma deposition process. For applying bias, a back Al contact layer and a top (transparent) indium-tin-oxide (ITO) electrode of 2x2.5 mm² are formed on samples to conduct (collect) an external bias (photocurrent) and to allow light transmission. A schematic structure of the photodetector is shown in **Fig 4.5**

Fig 4.6 shows current-voltage (*I-V*) characteristics of this ITO/nc-Si (nc-Ge) embedded MS/*p*-Si device without illumination. A rectifying ratio of 87 was measured at ± 3 V. In the range of low forward bias from 0 to 1 V, the *I-V* characteristic was fitted fairly using the equation given in Ref. 3 and presented in **Fig. 4.6** by series connection of a diode (ideality factor 20 (14) for nc-Si(Ge) embedded photodetector). Over this range, a bias dependence current ($\sim V^{2.03}$ and $V^{1.78}$ for Si and Ge) was obtained, indicating that space-charge-limited current dominates *I-V* characteristics.[4]

Very different *I-V* characteristics were observed at reverse bias. As shown in **Fig. 4.6**, for the bias >1.1 V, the originally very low reverse current (hereafter referred to as the dark current) increased drastically when the device was illuminated with light in the wavelength range of 340–1000 nm (only several typical curves are depicted here). The increase of photocurrent exhibited a linear dependence with increase of voltage at lower reverse bias until the current saturated to a value I_S at higher bias.

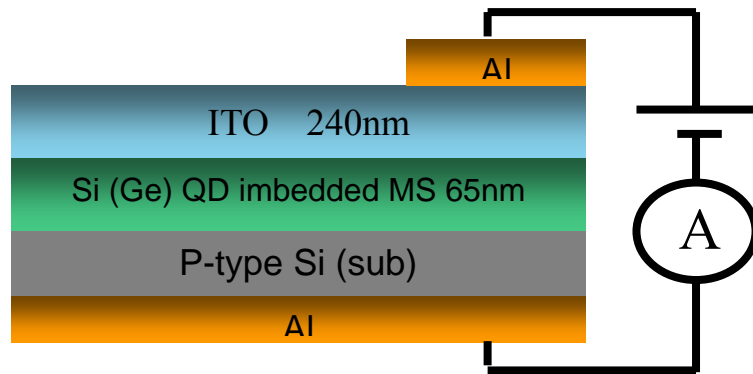


Fig 4.5 A schematic drawing illustrating the structure of the photodetector MS/ p-Si

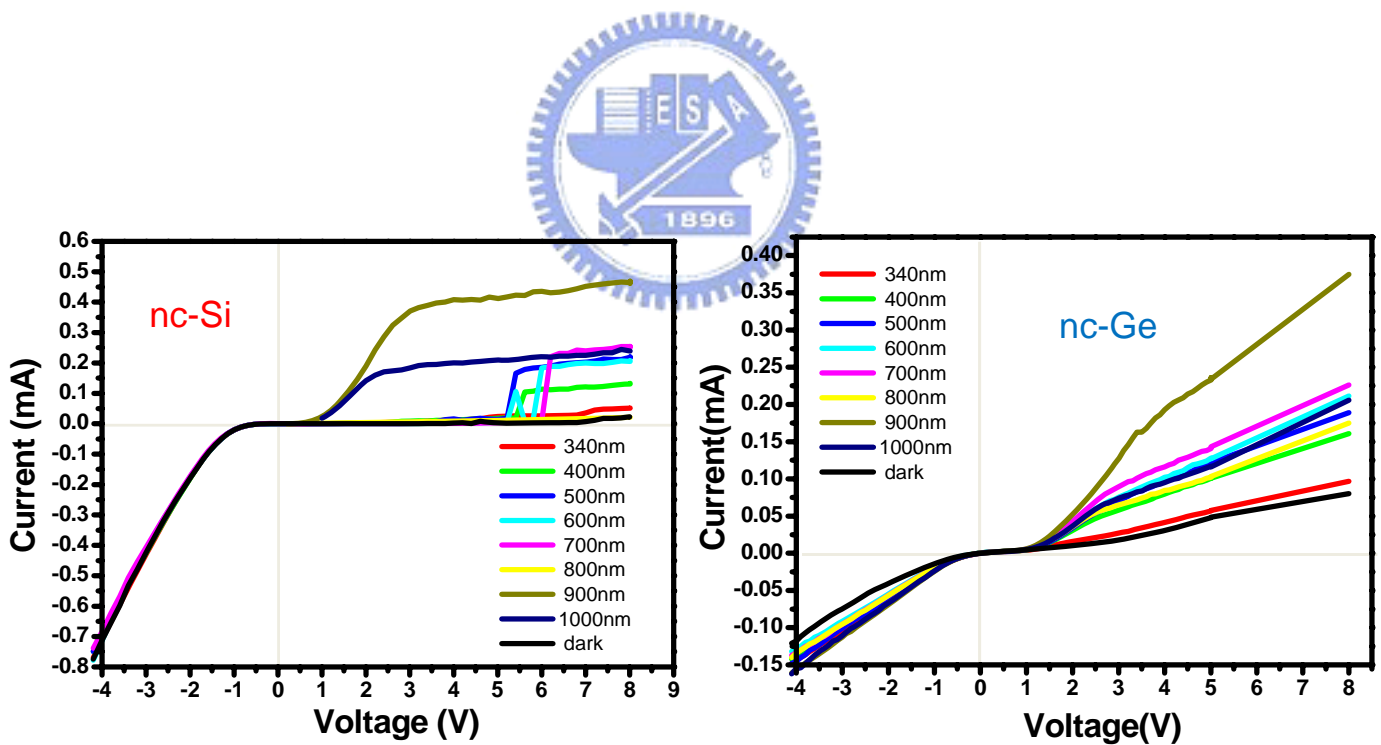


Fig 4.6 Current-voltage characteristics of (a) ITO/nc-Si-embedded MS/p-Si and (b) ITO/nc-Ge-embedded MS/p-Si devices under dark and under illumination at wavelength from 340 to 1000 nm.

4.4 Results of Spectral response

Fig. 4.7 summarizes the measured photoresponse over a wide range of incident light wavelengths for the ITO/nc-Si(Ge) embedded MS/*p*-Si MOS detectors at bias voltages of +8 V, together with a reference curve obtained for the same device structure but without nc doped, namely, ITO/MS/*p*-Si diodes. The photoresponse values plotted in the figure were calculated after subtracting the dark current at the corresponding bias. To compare with the effect of intrinsic absorption, typical spectral response for Si and Ge detectors were also shown [10]. Biased at +8 V, the photoresponse of an ITO/MS/*p*-Si structure increased essentially linearly with wavelength from 340 to 1000 nm by three times. The responsivity character of both nc-Si and nc-Ge distributed device were essentially the same. For the nc-Si doped sample, the responsivity were as high as 0.36, 0.7 and 0.9 A/W at 430, 560 and 790 nm, respectively. And for the nc-Ge doped sample, the responsivity were 0.3, 0.72 and 1 A/W at 420, 640 and 800 nm, respectively. The illumination intensity dependence of photocurrent in the device without nc-Si or nc-Ge distributed (ITO/MS/*p*-Si) was relatively small. As shown in **Fig.4.7**, the responsivity over the measured region (340~1000nm) was smaller than tenth of nc-Si (Ge) distributed device.

For convenience, a guideline was plotted in **Fig. 4.7**, representing the quantum efficiency value of 100%. We measured conversion efficiency values of more than 100% over the wavelength range of 530 to 970 nm, and as high as 138% (153%) at 800 nm for the ITO/nc-Si (Ge)-embedded MS/*p*-Si detector. Therefore, there must be an amplification mechanism to enhance the measured photoresponse at reverse bias. Furthermore, low dark currents with high dynamic resistance of 19.2 M Ω and high photoresponse yield high detectivity of 7.2×10^{12} cm Hz^{0.5}W⁻¹ for the present detector.[6]

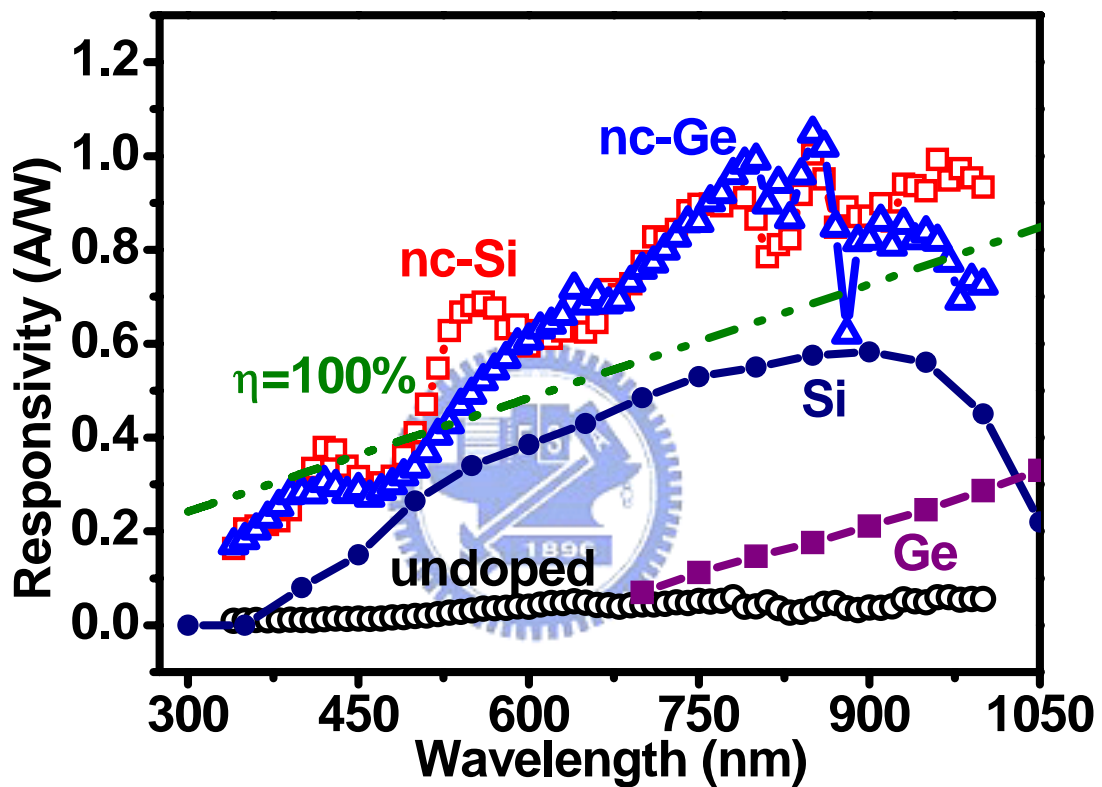


Fig 4.7 Spectral dependence of the photoresponse of detectors with ITO/nc-Si-embedded MS/ *p*-Si, ITO/nc-Si-embedded MS/ *p*-Si, ITO/MS/*p*-Si structures and typical spectral response for Silicon and Germanium. A guideline was plotted representing the quantum efficiency value of 100%.

4.5 Amplified current caused by barrier lowering of transistor

4.5.1 Bipolar junction transistor

We can gain a basic understanding of the operation of the transistor and the relations between the various and voltages by considering simplified analysis. The minority carrier concentrations are shown in Fig.4.8 for an npn bipolar transistor biased on the forward active mode. The electrons diffuse across the base are swept into the collector by the electric field in the B-C space charge region. Assuming the ideal linear electron distribution in the base, the collector current can be written as a diffusion current given by

$$i_c = I_s \exp\left(\frac{V_{BE}}{V_t}\right) \quad (4.1)$$

The collector current controlled by the base-emitter voltage; that is, the current amplify from barrier lowering of a BJT was caused by applied bias.

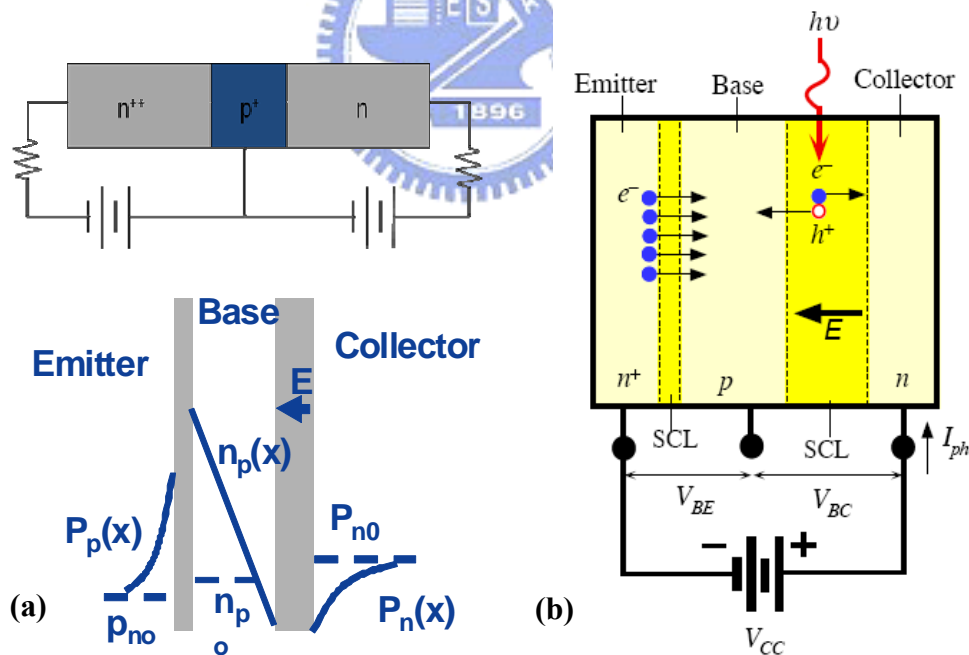


FIG. 4.8 (a) Biasing and carrier distribution of an npn BJT in the forward-active mode. (b) The principle of operation of the phototransistor. The primary photocurrent acts as a base current and give a large photocurrent in the emitter-collector circuit.

4.5.2 Phototransistor

The phototransistor [7] is a bipolar junction transistor (BJT) that operates as a photodetector with a photocurrent gain. The basic principle is illustrated in **Fig.4.8.(b)**. In an ideal device, only the depletions, or the space charge layers (SCL), contain an electric field. The base is terminally open and there is a voltage applied between the collector and emitter terminals just as in the normal operation of a common emitter BJT. An incident photon is absorbed in the SCL between the base and collector to generate an electron hole pair (EHP). The field E in the SCL separates the electron hole pair and drifts them in opposite direction. This is the primary photocurrent. When the drifting electron reaches the collector, it becomes collected (and thereby neutralized) by the battery. On the other hand, when the hole enters the neutral base region, it can only be neutralized by injecting a large number of electrons from the emitter into the base. These electrons diffuse across the base and reach the collector and thereby constitute an amplified photocurrent.

Alternatively, one can argue that the photogeneration of EHPs in the collector SCL decrease the resistance of this region which decreases the voltage V_{BC} across the base-collector junction. Consequently the base-emitter voltage V_{BE} must increase inasmuch as $V_{BE} + V_{BC} = V_{BC}$ (**Fig.4.8.(b)**). This increase in V_{BE} act as if it were a forward bias across the base-emitter junction and injects electrons into the base due to the transistor action, that is the emitter current

$$I_E \propto \exp(eV_{BE} / kT)$$

The current amplify from barrier lowing was caused by the incident photon in the space charge region.

4.5.3 Transistor-like mechanism

Based on the experimental evidence, we propose the following mechanism to explain why the detector efficiency could be more than 100% through this two-terminal detector with a nc-Si (or Ge)-embedded MS layer as the absorption medium. This is illustrated in **Fig. 4.9.(a)** Before illumination, the device operates like a normal MOS capacitor, i.e., a significant number of electrons are accumulated at the MS-Si interface forming a *n*-type inversion layer if a large enough reverse bias is applied. Only a few carriers could flow over the MS barrier layer, leading to a considerably low dark current. As seen in **Fig. 4.9. (b)**, upon optical excitation, strong absorption occurs for incident photons with the energies matching the transition energies from the ground hole states (E_h^0) to the ground electron states (E_e^0) (the gap energy between the highest occupied molecular orbital and the lowest unoccupied molecular orbital according to Ref 8, and the ground hole states (E_h^0) to the excited states (E_e^*) in connection to the Si-O interface states as well. With the applied electric field, the excited electrons in the E_e^0 and E_e^* states are driven towards the ITO contact layer via the tunneling process. The holes, however, will be trapped by the interface states [9] with the energy level somewhat above the ground hole states (E_h^0). The immobile positive charge centers will subsequently lower the barrier height, causing the resonant injection of electrons from the inversion layer through the MS layer to the ITO contact. Therefore, the measured photocurrent is expected to be composed of two parts, i.e., the photoexcited electrons plus the injected electrons. The mechanism of current amplification observed in this work is thus similar to that of a conventional phototransistor.[10] In particular, the enhancement of photoresponsivity measured between 530 and 970 nm, can be explained by the two resonant states of the nc-Si/MS system[8,9,11].

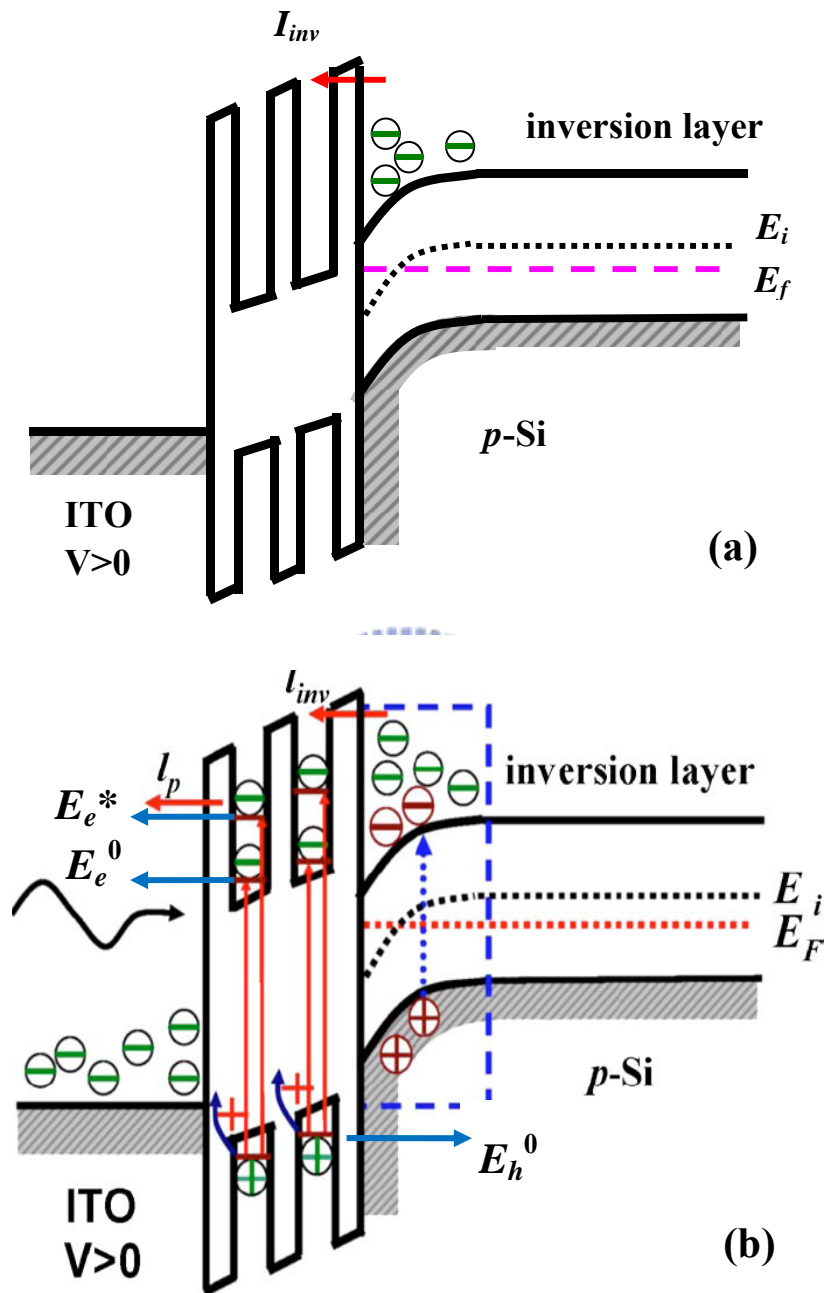


FIG. 4.9 Illustration of transistor like operation of an ITO/nc- Si-embedded MS/*p*-Si device under reverse bias. (a) A schematic band diagram before illumination and (b) under illumination. The symbols I_p and I_{inv} in the figure represent photoexcited and injected currents, respectively.

The situation is different when the gate bias is changed from positive to negative (**FIG. 4.10**). Although excited electrons in this case are expected to move to the side of the Si substrate, recombination with holes in the surface accumulation layer will significantly reduce the charge transport. At the same time, there will be little enhancement of hole transport from the MS layer to ITO, since the photogenerated holes are mostly trapped at the interface states. Therefore, the measured current would not differ too much from the case without photoexcitation.

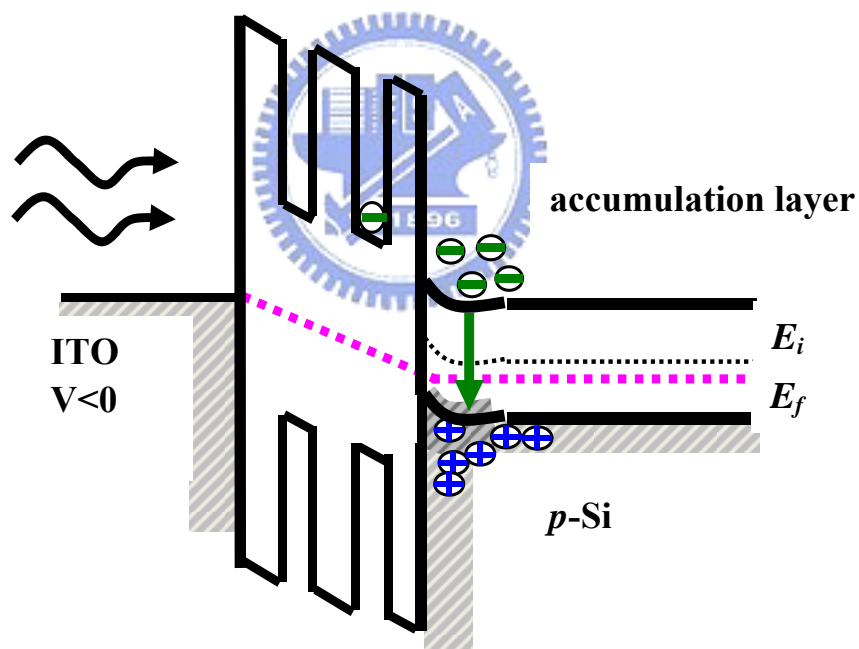


FIG. 4.10 A schematic band diagram of an ITO/ nc-Si(Ge)-embedded MS/ *p*-Si device under forward bias.

4.6 References

1. A. T. Cho, J. M. Shieh, J. Shieh, Y. F. Lai, B. T. Dai, F. M. Pan, H. C. Ku, Y.C.Lin, K. J. Chao, and P. H. Liu, *Electrochem. Solid-State Lett.* **8**, G143 (2005).
2. T. Z. Lu, a M. Alexe, R. Scholz, V. Talelaev, and M. Zacharias, *APL* **87**, 202110 (2005)
3. T. A. Burr, A. A. Seraphin, E. Werwa, and K. D. Kolenbrander, *Phys. Rev. B* **56**, 4818 (1997).
4. M. A. Rafiq, Y. Tsuchiya, H. Mizuta, S. Oda, Shigeyasu Uno, Z. A. K. Durrani, and W. I. Milne, *Appl. Phys. Lett.* **87**, 182101 (2005).
5. H. YAMAGISHI, Y. SUZUKI, A. HIRAIDE. *IEEE Transactions on Instrumentation and Measurement*, VOL 38, NO 2, (1989)
6. C. K. Wang, T. K. Ko, C. S. Chang, S. J. Chang, Y. K. Su, T. C. Wen, C. H. Kuo, and Y. Z. Chiou, *IEEE Photonics Technol. Lett.* **17**, 2161 (2005).
7. S.O.Kasap, *Optoelectronics and photonics*, p238
8. A. Puzder, A. J. Williamson, J. C. Grossman, and G. Galli, *Phys. Rev. Lett.* **88**, 097401 (2002).
9. S. H. Choi and R. G. Elliman, *Appl. Phys. Lett.* **74**, 3987 (1999).
10. A. Elfving, M. Larsson, G. V. Hansson, P.-O. Holtz, and W.-X. Ni, *Mater. Res. Soc. Symp. Proc.* **770**, I2.2 (2003).
11. M. V. Wolkin, J. Jorne, P. M. Fauchet, G. Allan, and C. Delerue, *Phys. Rev. Lett.* **82**, 197 (1999).

Chapter 5 Conclusions

5.1 Conclusions

By inductively coupled plasma chemical vapor deposition (**ICPCVD**), we dispersed three-dimensional dispersed Si nanocrystals (NCs) within the mesoporous silica films. ICP makes reactive species own highly mobile and bond with pore-wall well, therefore, efficiently construct 3D Si NCs/silica arrays. The mean density of ICP-synthesized NCs is as high as $\sim 10^{18}/\text{cm}^3$. And the multilevel charge storage (the steps in the flat-band shift) was caused by the charging of numerous layers of nc-Si(Ge). The specific interfacial bond-induced wide-bandgap electronic structure in nanostructured film significantly enhances the light extraction efficiency and the conduction of photoexcited carriers.

We demonstrated efficient UV to NIR ITO/nc-Si (or Ge) embedded MS/ *p*-Si detectors with enhanced photoresponse by thin film technology. The capping layer consisted of three-dimensional array of nanocrystals embedded in a mesoporous silica matrix was integrated in the IC-compatible configuration of metal-oxide-semiconductor structure. The device revealed a responsivity of 0.36, 0.7 and 0.9 A/W at 430, 560 and 790 nm for nc-Si doped sample. And 0.3, 0.72 and 1 A/W at 420, 640 and 800 nm for nc-Ge doped sample, respectively. Low dark currents with high dynamic resistance of $19.2 \text{ M}\Omega$ and high photoresponse gives high detectivity of $7.2 \times 10^{12} \text{ cm Hz}^{0.5}\text{W}^{-1}$.

The enhancement effect was explained by the transistorlike operation mechanism when the device was operated at reverse bias. The primary photocurrent generated in the nc-Si of the MS layer was amplified due to the electron injection from the inversion layer through the MS dielectric to the ITO contact. Therefore, the measured optoelectronic conversion efficiency can be more than 100% in the spectral range

between 530 and 970 nm and as high as 138% at 800 nm.

Comparing to the intrinsic absorption spectra of Silicon and Germanium, the responsivity character of nc-Si and nc-Ge distributed device were essentially the same. The photocurrent of the device without nc distributed (ITO/MS/ *p*-Si) was smaller than tenth of nc distributed sample. It was been explained that instead of intrinsic absorption, the connected Si-O surface states dominate the generation of electron-hole pair and enhances the light extraction efficiency and the conduction of photoexcited carriers.

